

**Percolated Strain Networks and Universal Scaling Properties of Strain Glasses**

Hongxiang Zong,<sup>1</sup> Haijun Wu,<sup>3</sup> Xuefei Tao,<sup>1</sup> Deqing Xue,<sup>1</sup> Jun Sun,<sup>1</sup> Stephen J. Pennycook,<sup>3</sup>  
 Tai Min,<sup>1</sup> Zhenyu Zhang,<sup>2,\*</sup> and Xiangdong Ding<sup>1,†</sup>

<sup>1</sup>*State Key Laboratory for Mechanical Behavior of Materials, Xi'an Jiaotong University, Xi'an 710049, China*

<sup>2</sup>*International Center for Quantum Design of Functional Materials (ICQD),*

*Hefei National Laboratory for Physical Sciences at Microscale,*

*and Synergetic Innovation Center of Quantum Information and Quantum Physics,*

*University of Science and Technology of China, Hefei, Anhui 230026, China*

<sup>3</sup>*Department of Materials Science and Engineering, National University of Singapore, 117574 Singapore*



(Received 11 October 2018; published 3 July 2019)

Strain glass is being established as a conceptually new state of matter in highly doped alloys, yet the understanding of its microscopic formation mechanism remains elusive. Here, we use a combined numerical and experimental approach to establish, for the first time, that the formation of strain glasses actually proceeds via the gradual percolation of strain clusters, namely, localized strain clusters that expand to reach the percolating state. Furthermore, our simulation studies of a wide variety of specific materials systems unambiguously reveal the existence of distinct scaling properties and universal behavior in the physical observables characterizing the glass transition, as obeyed by many existing experimental findings. The present work effectively enriches our understanding of the underlying physical principles governing glassy disordered materials.

DOI: [10.1103/PhysRevLett.123.015701](https://doi.org/10.1103/PhysRevLett.123.015701)

When a condensed matter system is cooled from its high-temperature liquid phase toward its freezing temperature, the system usually transforms into a crystalline solid [1]. However, when the cooling rate is not slow enough, the system may transform into a metastable glassy state, signified by the percolation and dominance of disordered regions [2,3]. The most commonly encountered glasses are structural glasses such as ceramic and metallic glasses; here, the atomic structures deviate severely from their respective crystalline phases [4,5]. Another major category of glasses is defined by physical observables other than their structural properties, such as spin or ferroelectric glasses associated with the magnetic or electric dipole moments, respectively [6,7]. Each class of glasses poses a broad range of standing challenges on their better fundamental understanding, and each class also has immense technological applications [8–11].

Among the second (or property) category, strain glass has been proposed as a conceptually intriguing and relatively new state of matter, which is inherently tied to the local field induced by crystal defects such as dopant atoms in host systems [12,13]. A crucial difference emerges between all the other (structural or property) glasses discussed above and the strain glass emphasized here: In the earlier systems, the introduction of dopants will certainly enlarge the phase space for glass formation, but it is not indispensable; in contrast, doping or other types of defect must be invoked for the formation of strain glasses [14–16]. It has been realized that the strain glass transition

can be influenced by dopants from two aspects: On one hand, dopant atoms can alter the global thermodynamic stability of martensite, which is often described as a chemical effect [5]; on the other hand, the creation of “random fields” dictates the development of martensite variants locally, termed the local field effect [17]. Theoretical models have utilized the two effects to capture aspects of the phase diagram and non-ergodic behavior [18]. Beyond this level of understanding, many fundamentally important questions remain, especially surrounding the underlying formation mechanism of strain glass at the atomic level.

In this Letter, we use a combined numerical and experimental approach to establish, for the first time, that the formation of strain glasses must proceed via the gradual percolation of strain clusters, namely, localized strain centers that expand to reach the percolating state. In essence, we preserve the original conceptual meaning of “strain glass,” but substantiate and enrich it with the present finding that it is signified by the percolation of the strain clusters through the strain network. Furthermore, our simulation studies of a wide variety of specific materials systems unambiguously reveal the existence of distinct scaling properties and universal behavior in the physical observables characterizing the glass transition, as obeyed by many existing experimental findings. These universal scaling properties may find transformative applicability in other types of glasses as well.

We first study the strain glass formation using molecular dynamics (MD) simulations of  $\text{Zr}_{100-x}\text{Ni}_x$  as a prototypical metallic alloy system, where  $x$  measures the dopant

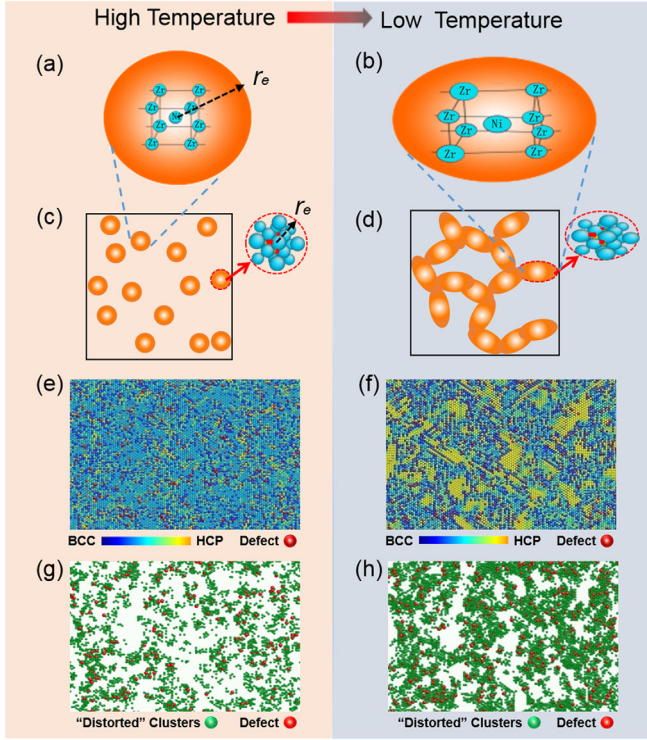


FIG. 1. Strain percolation and strain glass transition. (a)–(d) Schematic of the formation of strain network: randomly distributed point defect(s) induce strain cluster(s) (a),(c). The growth and connectivity of strain clusters upon cooling [(a) to (b); (c) to (d)] gives rise to the formation of a percolated strain network. The central effective dopant and other cluster atoms inside the dashed circles of 1(c) and 1(d) are colored by red and blue, respectively. (e)–(h) Results of molecular dynamics simulations, displaying typical atomic structures of strain glass with the martensitic regions colored yellow, parent phase regions colored blue and dopant atoms colored red (e),(f), and related strain clusters above and below the glass transition temperature (g),(h).

concentration (see Supplemental Material [19]). Without Ni dopants, clean Zr undergoes a phase transformation from cubic to hexagonal lattices accompanied by a structural symmetry change from  $Im\bar{3}m$  to  $P6_3/mmc$ . As illustrated in Fig. 1(a), each substitutional dopant will not change the global structural symmetry of crystal, but generates an anisotropic stress field [48], felt by a strain cluster characterized by a number of neighboring atoms within the average range of  $r_e$ . Because of thermal fluctuation effects,  $r_e$  is larger at lower temperatures. In addition, the strain clusters may also develop anisotropic shapes at lower temperatures, especially at and below the glass transition temperature.

The above features can both be captured by the dynamic pair distribution functions (DPDFs) [49], which are defined by  $G(r, t) = \langle \sum_i \sum_j \delta(r_j(t) - r_i(0) - r) \rangle$ , and  $G(r, \omega) = \int G(r, t) e^{i\omega t} dt$ , where  $r_i$  is the position of atom  $i$ ,  $t$  is the time delay, and  $\omega$  is the vibrational frequency. The DPDF enables us to identify the size and directions of

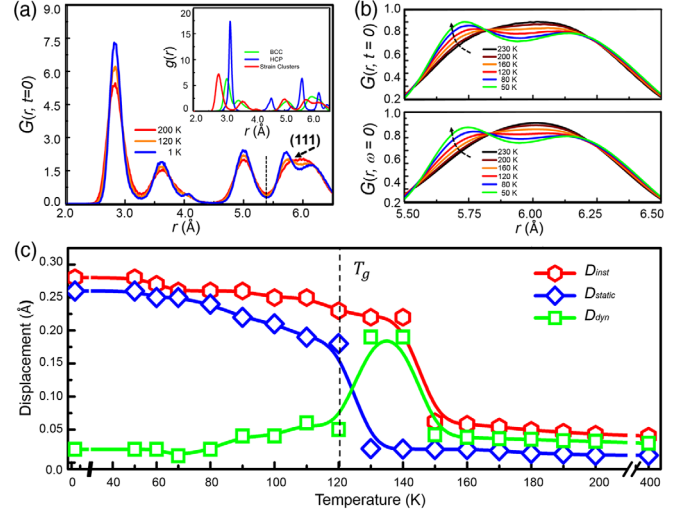


FIG. 2. Temperature dependence of the dynamic pair distribution function (DPDF). (a) The DPDF of Ni-Zr pairs showing peak splitting for the fourth neighbor in the course of the transition, indicating a local symmetry broken within the strain clusters. The inset show radial distribution function  $g(r)$  for the prototypical, martensitic, and strain cluster structures. (b) Instantaneous  $G(r, t = 0)$  and time-averaged  $G(r, \omega = 0)$  Ni-Zr DPDFs for the fourth peak, showing changes of lattice distortion with temperature. (c) The magnitude of the instantaneous peak shift  $D_{inst}$  and its static  $D_{static}$  and dynamic  $D_{dyn}$  components vs temperature.

displacement correlations as well as the atomic-scale local lattice distortions within the strain clusters during cooling. In this scenario, the instantaneous  $G(r, t = 0)$  is used to characterize the structural information at a particular moment while the static  $G(r, \omega = 0)$  is the time-domain average of  $G(r, t = 0)$ , related to the average structures that are independent of time.

Typical DPDFs are shown in Fig. 2. From Fig. 2(a) the Ni-Zr instantaneous  $G(r, t = 0)$  shows peak splitting for the fourth neighbors during the course of the glass transition, and becomes obvious at and below the glass transition temperature. The peaks of the DPDF presented in Fig. 2(b) correspond to the Ni-Zr cage and become asymmetric with positively skewed distributions for all the temperatures below  $T_g$ . It indicates a symmetry reduction in the Ni-Zr cages surrounding the dopant atoms, which is analogous to that taking place in the course of the PZT ferroelectric phase transition [50]. This change is quite different from that of the cubic to hexagonal phase transition. The radial distribution functions  $g(r)$  in the inset of Fig. 2(a) show that the strain clusters have a unique structure that differs from the parent phase and martensite, and are achieved via a shear along the  $\langle 111 \rangle$  direction (not a shear along the  $\langle 110 \rangle$  direction for the parent-martensite transition). Such anisotropic cages facilitate the formation of the strain networks. Unlike  $G(r, t = 0)$ , the time-averaged  $G(r, \omega = 0)$  shows almost symmetric peaks at high temperatures above  $T_g$ , indicating a small and temperature

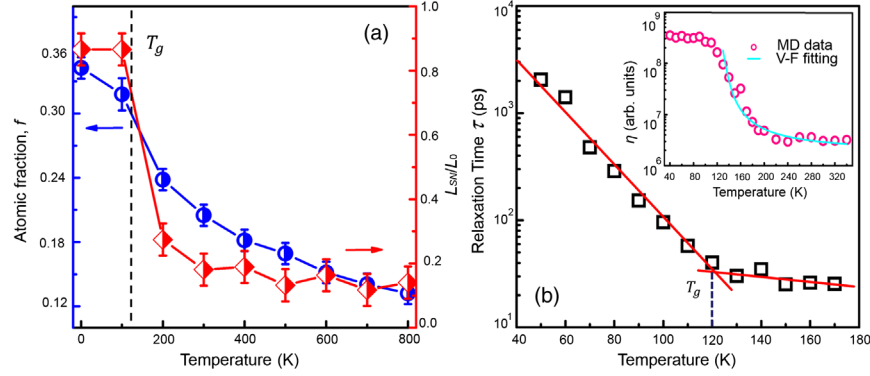


FIG. 3. Simulated properties during the glass transition of  $\text{Zr}_{96}\text{Ni}_4$ . (a) Spanning length  $L_{SN}$  of the largest network divided by the edge length  $L_0$  of the simulation supercell, and temperature dependence of the mole fraction of atoms  $f$  belonging to the strain networks. (b) Kinetic slowing down measured by the average relaxation time as a function of temperature, obtained by fitting the curves in the self-intermediate scattering function [19]. The inset shows the temperature dependence of the viscosity. The line above the glass transition temperature is fitted by the Vogel-Fulcher law  $\eta = \eta_0 e^{E/k_B(T-T_{VF})}$  with the reference viscosity  $\eta_0 = 1.72 \times 10^6$ , Boltzmann constant  $k_B$ , Vogel-Fulcher temperature  $T_{VF} = 108$  K and activation energy  $E/k_B = 102$  K.

independent time-averaged lattice distortion. Next, we use the magnitude of the peak shift to quantify the size of the strain clusters. The static component  $D_{\text{static}}$  is obtained from the peak shift of  $G(r, \omega = 0)$  in Fig. 2(b), while the dynamic component  $D_{\text{dyn}}$  is defined as the difference between the instantaneous peak shift  $D_{\text{inst}}$  [the peak shifts of  $G(r, t = 0)$ ] and  $D_{\text{static}}$ . As shown in Fig. 2(c), strain clusters can dynamically appear (green curve) above the glass transition temperature. Approaching  $T_g$ , the size of stable strain clusters (blue curve) increases rapidly then starts to saturate below  $T_g$ . Accordingly, atoms within the strain clusters are identified with  $D_{\text{static}}$  greater than the value at  $T_g$ .

Beyond the behavior of an individual strain cluster, cluster-cluster interaction becomes significant at a given dopant concentration but lower temperatures, or at a given temperature but higher concentrations. In particular, when the strain clusters percolate, the system starts to transition into the strain glass state, as conceptually illustrated in Figs. 1(c) and 1(d). Here, it is important to emphasize that both the enlarged size and the emerging anisotropy of the strain clusters at low temperatures play an important role in reaching the transition state. Our detailed MD results are shown in Figs. 1(e)–1(h) at two representative limiting temperatures. From Figs. 1(e) and 1(g), we observe the absence of percolated order in either the atomic configuration [Fig. 1(e)] or the strain clusters [Fig. 1(g)] of the system at the high temperature of 400 K. In contrast, at the very low temperature of 1 K, the martensitic domains clearly lack long-range order [Fig. 1(f)], while the strain clusters exhibit distinct percolated nature [Fig. 1(g)], thereby signifying the potential existence of a strain glass transition, with the precise transition temperature to be determined within the two limits. Here, we note that Fig. 1 only highlights the dominant strain clusters and the percolated strain network, downplaying the unstrained parent phase, which occupies only a low volume fraction (typically

less than 15%, Fig. S2 [19]). Furthermore, the lattice distortion in the percolated network is rather low, explaining why normal x-ray diffraction still observes the parent phase, while the higher resolution synchrotron x-ray diffraction will be able to resolve the structural change [13,14].

Now we address the crucial issue, namely, the existence of the strain glass transition, using two complementary approaches. The first is to quantitatively establish the emergence of percolation of the strain clusters beyond the visual indication shown in Fig. 1(h), by calculating the total fraction of atoms  $f$  belonging to the strain clusters. At the given dopant concentration of  $x = 4$  at. % as used in Figs. 1(e)–1(h), we find that  $f$  increases slowly as the temperature decreases, but more sharply at  $T_g = 120$  K [Fig. 3(a)], indicating the emergence of a characteristic percolating transition. The corresponding  $f_{T_g} = 0.283$ , which is distinctly above the site percolation threshold for ideal bcc lattices containing random dopants ( $f_c = 0.246$ ). This observation of the glass transition is again corroborated by another measure  $L_{SN}$ , the linear dimensional length of the largest strain cluster network. As shown in Fig. 3(a),  $L_{SN}/L_0$  rises more pronounced at the percolation threshold, as it should be; here  $L_0$  is the dimensional length of the simulation cell [30,51].

The second approach is to reproduce the salient features of glassy materials. The characteristic relaxation time ( $\tau$ ) of the system with the same  $x = 4$  at. % starting from an initial perturbed configuration towards the corresponding equilibrium state at different temperatures is first quantified. Here,  $\tau$  is defined by the decay of the self-intermediate scattering function  $F_S(\vec{q}, t)$  from the initial value of unity to  $1/e$  [52]. The results are shown in Fig. 3(b), displaying two drastically different regions separated by the glass transition temperature  $T_g$ . In particular, we see orders of magnitude slowing down in the relaxation kinetics below  $T_g$ , which is typically observed experimentally in

strain glasses such as  $\text{Ti}_{48.5}\text{Ni}_{51.5}$  [53]. As a complementary, the temperature evolution of the viscosity  $\eta$  fits the Vogel-Fulcher law very well [the inset of Fig. 3(b)], indicating that the strain glasses share great similarity with the fragile structural glasses [54].

Next, we explore the strain glass transition at different dopant concentrations. For a given system, there exists a critical dopant concentration  $x_c$ , below which no strain glass can be formed [12,17]. As approaching  $x_c$ , the glassy behavior becomes weaker, while the dependence on the cooling rate becomes stronger [55]. In contrast, the glass formation ability is much stronger far above  $x_c$ , while the dependence on the cooling rate becomes much weaker. For a given cooling rate,  $x_c$  depends on the strength of the local strain distribution, smaller for stronger strain. For the  $\text{Zr}_{100-x}\text{Ni}_x$  systems, at the same cooling rate of  $10^{11}$  K/s,  $x_c$  is determined to be  $\sim 3.5$  at. % (Fig. S4 [19]). Before we proceed further on the MD studies, we use the specific material systems of  $\text{Ti}_{50}\text{Pd}_{50-x}\text{Cr}_x$  to confirm experimentally the existence of strain cluster percolation in a strain glass above the critical dopant concentration. Detailed experimental procedures are described in [19]. The results are given in Fig. 4, displaying the (scanning) transmission electron microscopy (TEM or STEM) images of the martensite system  $\text{Ti}_{50}(\text{Pd}_{42}\text{Cr}_8)$  [Fig. 4(a)], the crossover system  $\text{Ti}_{50}(\text{Pd}_{41}\text{Cr}_9)$  [Fig. 4(b)], and the strain glass system  $\text{Ti}_{50}(\text{Pd}_{40}\text{Cr}_{10})$  [Fig. 4(c)]. The diffusive superlattice of the strain glass is a characteristic feature of the nanodomains with the loss of long-range ordering. The cross-linked nanodomains are formed with a high density of local lattice distortions, as shown in the high-resolution (HRTEM) images of Figs. 4(d) and S8(a), and the STEM annular bright-field (ABF) image of Fig. S9(a); these lattice distortions further induce connected strain network. To investigate strain variations within the nanodomains, the HRTEM and STEM ABF images are analyzed through geometric phase analysis (GPA) [23], as shown in Fig. 4(e) and Figs. S8(b)–S8(f), S9(b)–S9(f), and S10 [19]. The strained clusters with a maximum lattice distortion of  $\sim 5\%$  embedded in the matrix with low distortion connect to form the percolated strain network. Here, it is to be noted that, in essence, this is the first experimental observation of the percolation of strain clusters in a strain glass state, which validates the main findings from the MD simulations presented earlier for the prototypical system.

Now we return to the MD studies of the strain glass transition, focusing more on revealing general trends and universal behaviors beyond one specific host system. The first is to establish the existence of a subtle and important general trend in the cooperative rule of cluster-cluster interaction in different classes of systems that may harbor strain glass transitions. We introduce the average number ( $n_r$ ) of atoms contained within an isolated strain cluster induced by a dopant atom, and the total fraction of atoms ( $N_r$ ) contained within all the strain clusters of the system.

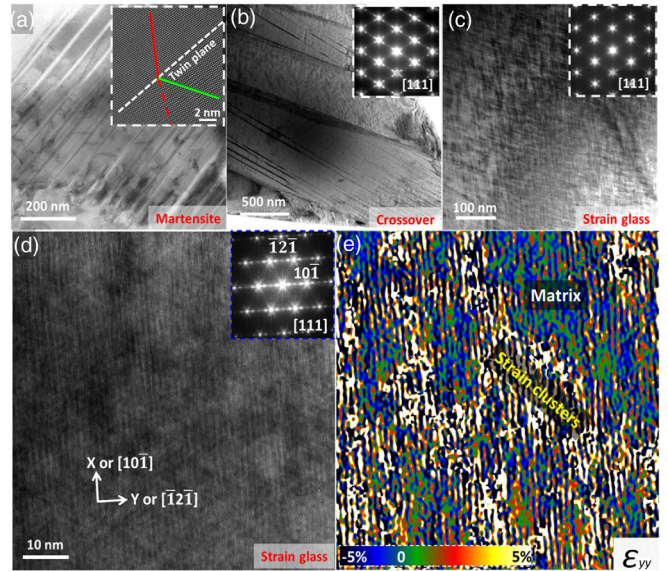


FIG. 4. Experimentally observed structural and strain networks. (a)–(d) Structural identification: (a) Low-magnification STEM ABF image of  $\text{Ti}_{50}(\text{Pd}_{42}\text{Cr}_8)$  at the martensite phase showing large-scale domains, with a high-magnification STEM HAADF image showing a twin boundary (inset). (b) TEM image of  $\text{Ti}_{50}(\text{Pd}_{41}\text{Cr}_9)$  at the crossover transition showing hierarchical nanodomain architecture, with an electron diffraction pattern showing sharp superlattices of the martensite phase (inset). (c) TEM image of  $\text{Ti}_{50}(\text{Pd}_{40}\text{Cr}_{10})$  at the strain glass transition, with an electron diffraction pattern showing diffusive superlattices of the martensite phase (inset). (d) Atomically resolved HRTEM image of  $\text{Ti}_{50}(\text{Pd}_{40}\text{Cr}_{10})$ , with FFT image inset. (e) GPA results of (d), namely the component  $\epsilon_{yy}$  of the strain, displaying the onset of percolated strain clusters in the strain glass state.

If cluster-cluster interaction is negligible, we should have  $N_r/n_r \sim x^\alpha$ , with  $\alpha = 1$ . Through detailed simulation studies of four metallic alloys with varying dopant concentrations,  $\text{Zr}_{100-x}\text{Ni}_x$ ,  $\text{Zr}_{100-x}\text{Al}_x$ ,  $\text{Zr}_{100-x}\text{Cu}_x$ , and  $\text{Ti}_{50-x}\text{Ni}_{50+x}$ , we find  $\alpha$  is distinctly greater than 1, as shown in Fig. 5(a), signifying the importance of cluster-cluster interaction. Strikingly, when we extract the  $N_r/n_r$  ratios of many experimentally identified strain glass systems, we find that such data can all be represented by the same scaling law of  $N_r/n_r \sim x^\alpha$ , with a universal and well-defined scaling exponent of  $\alpha = 1.2$ . The calculation details are given in [19]. It is intriguing to observe that the scaling exponent of 1.2 established here shares commonality with that in avalanche statistics [56], potentially suggesting broader significance of such results.

Finally, we exploit the enabling power of the universal scaling law shown in Fig. 5(a) in reaching a generic phase diagram of strain glass transitions of many systems, including the present simulated and existing experimental ones. Here, the chemical effect is rationalized by the doping induced change in the enthalpy of mixing as it governs the stability of competing phases and is more accessible experimentally [57,58]. Based on the

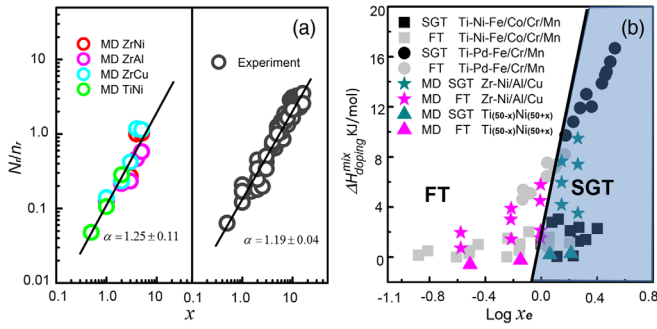


FIG. 5. Universal scaling behavior and generic phase diagram. (a) Power-law scaling of  $N_r/n_r$  vs the doping level  $x$  for a wide variety of doped ferroelastic alloys from both MD simulations and experimental measurements. The exponents are fitted via the maximum likelihood method. (b) Phase diagram spanned by  $\Delta H_{\text{doping}}^{\text{mix}}$  and  $x_e$  for doped ferroelastic alloys. In (b), the solid line is the result of a classification fit of the atomistic simulation data. The fitted line effectively separates the ferroelastic transition (FT) and strain glass transition (SGT) of the experimental data.

regular melt model [59,60], the mixing enthalpy of a doped ferroelastic alloy  $\Delta H_{\text{doping}}^{\text{mix}}$  is determined as  $\Delta H_{\text{doping}}^{\text{mix}} = \sum_{i \neq j, i=1}^3 4\Delta H_{ij}^{\text{mix}} c_i c_j$ , where  $\Delta H_{ij}^{\text{mix}}$  is the mixing enthalpy of binary liquid alloys with the  $i$  th and  $j$  th elements, and the values can be obtained from Ref. [35]. Simultaneously, we introduce another parameter, effective dopant concentration  $x_e = n_r x^\alpha$  (proportional to  $N_r$ ), which is used to qualify the local field effect induced by strain clusters or networks. This is shown in Fig. 5(b), with the phase diagram spanned by the enthalpy of mixing  $\Delta H_{\text{doping}}^{\text{mix}}$  and the effective dopant concentration  $x_e$ . Detailed simulations of two classes of metallic alloyed systems with varying dopant concentrations show that all these systems fall into two distinctly different regions separated by the boundary between the phases without and with strain glasses. Most strikingly, all the existing experimentally observed strain glass systems are also shown to be governed by the same phase diagram.

Figure 5(b) shows that strain glass is favored with higher  $x_e = n_r x^\alpha$ . Here,  $n_r$  is correlated with the ratio of the atomic radii between the solute and solvent atoms, and is anticorrelated with the elastic anisotropy [19]. It is consistent with the findings in previous Ginzburg-Landau theoretical model studies, which revealed a reduction of the elastic anisotropy suppresses the development of long-range order ferroelastic states [5,61].

In summary, using both numerical and experimental approaches, we have provided the first demonstration of the existence of percolating strain clusters in dopant ferroelastic alloys, convincingly establishing that strain glass shares the same commonality of percolation with other types of glasses. The strength of the percolating strain clusters can be exploited as a quantitative measure of the effective dopant concentration in revealing universal scaling properties of the strain glass transition, with the same

scaling exponent of 1.2 and a unified phase diagram for different glass forming systems. The scaling behavior can be regarded as the corollary of a percolating transition, as obeyed by a wide variety of strain glass materials, including simulated and experimentally observed ones, and is expected to find transformative applicability in other classes of glassy materials.

We acknowledge financial support of this work through grants from the National Natural Science Foundation of China (No. 51320105014, No. 51621603, No. 51871177) and the 111 project 2.0 (BP2018008). Z. Z. was partially supported by the National Key R&D Program of China (Grants No. 2017YFA0303503 and No. 2014CB921103) and the National Natural Science Foundation of China (No. 11634011, No. 61434002).

\*To whom all correspondence should be addressed.  
zhangzy@ustc.edu.cn

†To whom all correspondence should be addressed.  
dingxd@mail.xjtu.edu.cn

- [1] E. Woo, J. Huh, Y. G. Jeong, and K. Shin, *Phys. Rev. Lett.* **98**, 136103 (2007).
- [2] C. A. Angell, *Science* **267**, 1924 (1995).
- [3] D. Z. Chen, C. Y. Shi, Q. An, Q. Zeng, W. L. Mao, R. W. Goddard, and J. R. Greer, *Science* **349**, 1306 (2015).
- [4] Y. C. Hu, F. X. Li, M. Z. Li, H. Y. Bai, and W. H. Wang, *Nat. Commun.* **6**, 8310 (2015).
- [5] P. Lloveras, T. Castán, M. Porta, A. Planes, and A. Saxena, *Phys. Rev. Lett.* **100**, 165707 (2008).
- [6] B. E. Vugmeister and M. D. Glinchuk, *Rev. Mod. Phys.* **62**, 993 (1990).
- [7] K. Binder and A. P. Young, *Rev. Mod. Phys.* **58**, 801 (1986).
- [8] P. G. Debenedetti and F. H. Stillinger, *Nature (London)* **410**, 259 (2001).
- [9] H. W. Sheng, W. K. Luo, F. M. Alamgir, J. M. Bai, and E. Ma, *Nature (London)* **439**, 419 (2006).
- [10] J. Hemberger, P. Lunkenheimer, R. Fichtl, H. A. K. V. Nidda, V. Tsurkan, and A. Loidl, *Nature (London)* **434**, 364 (2005).
- [11] Y. H. Liu, G. Wang, R. J. Wang, D. Q. Zhao, M. X. Pan, and W. H. Wang, *Science* **315**, 1385 (2007).
- [12] S. Sarkar, X. Ren, and K. Otsuka, *Phys. Rev. Lett.* **95**, 205702 (2005).
- [13] Y. Zhou, D. Xue, X. Ding, K. Otsuka, J. Sun, and X. Ren, *Appl. Phys. Lett.* **95**, 151906 (2009).
- [14] R. Vasseur, D. Xue, Y. Zhou, W. Ettoumi, X. Ding, X. Ren, and T. Lookman, *Phys. Rev. B* **86**, 184103 (2012).
- [15] Y. Zhou, D. Xue, X. Ding, K. Otsuka, J. Sun, and X. Ren, *Phys. Status Solidi B* **251**, 2027 (2014).
- [16] S. Kirkpatrick and D. Sherrington, *Phys. Rev. B* **17**, 4384 (1978).
- [17] D. Wang, Y. Wang, Z. Zhang, and X. Ren, *Phys. Rev. Lett.* **105**, 205702 (2010).
- [18] D. Wang, X. Ke, Y. Wang, J. Gao, Y. Wang, L. Zhang, S. Yang, and X. Ren, *Phys. Rev. B* **86**, 054120 (2012).
- [19] See Supplemental Material at <http://link.aps.org/supplemental/10.1103/PhysRevLett.123.015701> for

- HRTEM experimental setup details and results, a description of the MD simulation details, relaxation time, viscosity, theoretical model for the size of strain clusters as well as power-law fitting, which includes Refs. [20–47].
- [20] J. Deng, X. Ding, T. Lookman, T. Suzuki, K. Otsuka, J. Sun, A. Saxena, and X. Ren, *Phys. Rev. B* **81**, 220101 (2010).
- [21] M. S. Daw and M. I. Baskes, *Phys. Rev. B* **29**, 6443 (1984).
- [22] L. Gao, X. Ding, H. Zong, T. Lookman, J. Sun, X. Ren, and A. Saxena, *Acta Mater.* **66**, 69 (2014).
- [23] M. J. Hytch, E. Snoeck, and R. Kilaas, *Ultramicroscopy* **74**, 131 (1998).
- [24] Y. Zhou, D. Xue, Y. Tian, X. Ding, S. Guo, K. Otsuka, J. Sun, and X. Ren, *Phys. Rev. Lett.* **112**, 025701 (2014).
- [25] L. Leuzzi and Th. M. Nieuwenhuizen, *Thermodynamics of the Glassy State* (Taylor & Francis, London, 2007).
- [26] J. D. Eaves and D. R. Reichman, *Proc. Natl. Acad. Sci. U.S.A.* **106**, 15171 (2009).
- [27] G. R. Barsch and J. A. Krumhansl, *Metall. Trans. A* **19**, 761 (1988).
- [28] W. Cai, R. B. Sills, D. M. Barnett, and W. D. Nix, *J. Mech. Phys. Solids* **66**, 154 (2014).
- [29] Z. P. Lu, H. Tan, S. C. Ng, and Y. Li, *Scr. Mater.* **42**, 667 (2000).
- [30] M. Sahimi, *Applications of Percolation Theory* (Taylor & Francis, London, 1994).
- [31] S. E. Rowley, T. Vojta, A. T. Jones, W. Guo, J. Oliveira, F. D. Morrison, N. Lindfield, E. Baggio Saitovitch, B. E. Watts, and J. F. Scott, *Phys. Rev. B* **96**, 020407(R) (2017).
- [32] M. J. Hytch, *Microsc. Microanal.* **8**, 41 (1997).
- [33] K. Otsuka and X. Ren, *Prog. Mater. Sci.* **50**, 511 (2005).
- [34] W. Cai, C. Tan, T. Shen, and X. Tian, *J. Alloy Compd.* **438**, 30 (2007).
- [35] A. Takeuchi and A. Inoue, *Mater. Trans.* **46**, 2817 (2005).
- [36] Z. Zhang, O. Elkedim, M. Balcerzak, M. Jurczyk, and R. Chassagnon, *Int. J. Hydrogen Energy* **42**, 23751 (2017).
- [37] O. N. Senkov and D. B. Miracle, *Mater. Res. Bull.* **36**, 2183 (2001).
- [38] Y. Zhou, D. Xue, X. Ding, Y. Wang, J. Zhang, Z. Zhang, D. Wang, K. Otsuka, J. Sun, and X. Ren, *Acta Mater.* **58**, 5433 (2010).
- [39] S. E. Kulkova, A. V. Bakulin, Q. M. Hu, and R. Yang, *Mater. Today Proc.* **2**, S615 (2015).
- [40] Y. Kishi, Z. Yajima, K. Shimizu, and K. Morii, *Mater. Sci. Forum* **327**, 123 (2000).
- [41] D. Wang, Z. Zhang, J. Zhang, Y. Zhou, Y. Wang, X. Ding, Y. Wang, and X. Ren, *Acta Mater.* **58**, 6206 (2010).
- [42] D. K. Rai, T. P. Yadav, V. S. Subrahmanyam, and O. N. Srivastava, *J. Alloys Compd.* **482**, 28 (2009).
- [43] X. Ren, N. Miura, J. Zhang, K. Otsuka, K. Tanaka, M. Koiwa, T. Suzuki, Y. I. Chumlyakov, and M. Asai, *Mater. Sci. Eng. A* **312**, 196 (2001).
- [44] M. Nishida, T. Hara, Y. Morizono, A. Ikeya, H. Kijima, and A. Chiba, *Acta Mater.* **45**, 4847 (1997).
- [45] X. Q. Chen, C. L. Fu, and J. R. Morris, *Intermetallics* **18**, 998 (2010).
- [46] S. M. Shapiro, B. L. Winn, D. L. Schlagel, T. Lograsso, and R. Erwin, *J. Phys. IV* **112**, 1047 (2003).
- [47] Y. Zhou, D. Xue, X. Ding, K. Otsuka, J. Sun, and X. Ren, *Phys. Status Solidi B* **251**, 2027 (2014).
- [48] K. Martens, L. Bocqueta, and J. Barrat, *Soft Matter* **8**, 4197 (2012).
- [49] B. Widom, *J. Chem. Phys.* **39**, 2808 (1963).
- [50] H. Takenaka, I. Grinberg, and A. M. Rappe, *Phys. Rev. Lett.* **110**, 147602 (2013).
- [51] Y. Sun, Z. Ye, F. Zhang, Z. J. Ding, C. Z. Wang, M. Kramer, and K. M. Ho, *Model. Simul. Mater. Sci. Eng.* **26**, 015006 (2018).
- [52] J. D. Eaves and D. R. Reichman, *Proc. Natl. Acad. Sci. U.S.A.* **106**, 15171 (2009).
- [53] Y. Wang, X. Ren, K. Otsuka, and A. Saxena, *Phys. Rev. B* **76**, 132201 (2007).
- [54] L. Berthier and G. Biroli, *Rev. Mod. Phys.* **83**, 587 (2011).
- [55] Y. Ji, D. Wang, X. Ding, K. Otsuka, and X. Ren, *Phys. Rev. Lett.* **114**, 055701 (2015).
- [56] A. Nicolas, E. E. Ferrero, K. Martens, and J. Barrat, *Rev. Mod. Phys.* **90**, 045006 (2018).
- [57] E. Perim *et al.*, *Nat. Commun.* **7**, 12315 (2016).
- [58] W. X. Song and S. J. Zhao, *J. Chem. Phys.* **142**, 144504 (2015).
- [59] Y. Zhang, Y. J. Zhou, J. P. Lin, G. L. Chen, and P. K. Liaw, *Adv. Eng. Mater.* **10**, 534 (2008).
- [60] A. R. Miedema, P. F. D. Châtel, and F. R. D. Boer, *Physica (Amsterdam)* **100B+C**, 1 (1980).
- [61] P. Lloveras, T. Castán, M. Porta, A. Planes, and A. Saxena, *Phys. Rev. B* **80**, 054107 (2009).